Journal of Solid State Chemistry 296 (2021) 121947

Contents lists available at ScienceDirect

Journal of Solid State Chemistry

journal homepage: www.elsevier.com/locate/jssc

Single crystal growth and characterization of new Zintl phase $Ca_9Zn_{3.1}In_{0.9}Sb_9$

David M. Smiadak [a], Sviatoslav Baranets [b], Megan Rylko [a], Mack Marshall [a], Mario Calderón-Cueva [a], Svilen Bobev [b,*], Alex Zevalkink [a,**]

[a] Department of Chemical Engineering and Materials Science, Michigan State University, East Lansing, MI, 48824, USA
[b] Department of Chemistry and Biochemistry, University of Delaware, Newark, DE, 19716, USA

ARTICLE INFO

Keywords:
Zintl phases
Crystal structure
Electronic structure
Single crystal X-ray diffraction
Thermoelectrics
Flux growth

ABSTRACT

Complex Zintl phases have yielded a large variety of promising new thermoelectric materials. In this study we report the discovery of the new Zintl phase $Ca_9(Zn_{1-x}In_x)_4Sb_9$ ($x \sim 0.9$), needle-like crystals of which were serendipitously obtained from an In- and Sb-rich flux. Although its composition is reminiscent of $Ca_9Zn_{4+x}Sb_9$, an excellent thermoelectric material with $zT > 1$, the substitution of In on the Zn site leads to the formation of an entirely new structure type. Single crystal X-ray diffraction revealed a structure characterized by TSb_4 tetrahedra (T = statistically disordered Zn and In atoms) and $ZnSb_3$ triangular units, which share common corners to form $[T_4Sb_9]^{18-}$ polyanions. The average structure was found to have hexagonal symmetry. The valence electron count in this heavily-disordered structure appears to follows the Zintl-Klemm rules, suggesting semiconducting behavior. Single crystal electrical conductivity and Seebeck coefficient measurements support this conclusion, suggesting that the as-grown crystals are degenerate *p*-type semiconductors.

1. Introduction

In recent years, there have been numerous reports on ternary pnictides in the *AE*–*Tr*–*Pn* (*AE* = Ca, Sr, Ba, Eu, Yb; *Tr* = Al, Ga, In; and *Pn* = As, Sb, Bi) systems and their potential use in thermoelectrics [1]. Examples include Ca_3AlSb_3 [2,3], $Ca_{11}TrSb_9$ [4], $Ca_5Tr_2Sb_6$ [5–8] and $AE_{14}TrSb_{11}$ [9], to name a few. Almost exclusively, such compounds can be classified as Zintl phases, where the alkaline-earth metals are treated as cations, and the post-transition elements use the donated electrons to form covalent bonds within polyanionic substructures of various dimensionality [10]. Through mixed bonding character and complex unit cells, Zintl phases achieve inherently low lattice thermal conductivities [11] and all constituent atoms achieve closed-shell configurations making the above-named compounds intrinsic small-gap semiconductors or semimetals. These are desirable characteristics in the development of thermoelectrics, and many research groups are turning their attention to Zintl phases as candidate materials for solid-state energy conversion [1,9,12].

Our research groups have previously explored much of the phase space within the ternary *AE*–Ga–Sb, *AE*–In–Sb, and *AE*–Zn–Sb phase diagrams (*AE* = Ca, Sr, Ba, Eu and Yb) [12–19]. From this work, the scope has been expanded to quasi-quaternary systems. For the synthesis of new compounds with novel structures, by and large, we have focused on the metal flux method [20] for its ability to form single crystals of a wide variety of compounds including incongruently melting species [21]. Previous work on the Ca–In–Sb system yielded $Ca_5In_2Sb_6$ single crystals from an In and Sb flux. In an effort to increase *p*-carrier concentration, small amounts of Zn were introduced to the flux in an effort to Zn-dope $Ca_5In_2Sb_6$. This led instead to the formation of the new $Ca_9(Zn_{1-x}In_x)_4Sb_9$ compound. Herein, we present the first attempts to fully characterize this new material, whose average structure bears similarities to other thermoelectric materials including $Ca_9Zn_{4+x}Sb_9$ [13,22], which is an excellent thermoelectric material with $zT \sim 1.2$. We report the bonding character of $Ca_9(Zn_{1-x}In_x)_4Sb_9$ along with the topological relationships to the structures of compounds mentioned above, and present the electronic transport properties measured on as-grown crystals.

* Corresponding author.
** Corresponding author.
E-mail addresses: bobev@udel.edu (S. Bobev), alexzev@msu.edu (A. Zevalkink).

https://doi.org/10.1016/j.jssc.2020.121947
Received 24 November 2020; Received in revised form 21 December 2020; Accepted 27 December 2020
Available online 6 January 2021

2. Experimental

2.1. Synthesis

Starting materials consisted of high purity elements: Ca (dendritic pieces, Sigma-Aldrich 99.9%), In (shot, Alfa Aesar 99.9995%), Sb (shot, Alfa Aesar 99.999%), and Zn (shot, Alfa Aesar 99.999%). Polycrystalline $Ca_5In_2Sb_6$ was synthesized as a precursor for flux growth using ball milling and spark plasma sintering. The elements were ball-milled in 5 g batches within a stainless steel jar containing two stainless steel balls (dia. = 12.7 mm) in a SPEX MixerMill 8000D for 60 min. The powder was then loaded into 10 mm graphite die sets (POCO EDM-3) with graphite foil spacers and spark plasma sintered in a Dr. Sinter 211LX system under vacuum. Samples were heated to 823 K in 5 min and held at temperature for 10 min to achieve the phase-pure precursor $Ca_5In_2Sb_6$.

The $Ca_9(Zn_{1-x}In_x)_4Sb_9$ crystals were serendipitously obtained from mixed-metal flux reaction that was initially intended to produce Zn-doped $Ca_5In_2Sb_6$ crystals. The initial loading used a starting mixture of polycrystalline $Ca_5In_2Sb_6$ and elemental In, Zn, and Sb ($Ca_5In_2Sb_6 + Zn_5 + In_{93} + Sb_{58}$). These precursors were then loaded into alumina Canfield crucible sets [21] which were sealed in fused silica ampules under vacuum ($<1 \times 10^{-4}$ torr). Next, growths were heated to 1173 K in 12 h, held at temperature for 2 h, and then cooled to 1000 K at a rate of 3 K/h. Ampules were extracted, flipped, and centrifuged at 2500 RPM for 2 min.

The above was determined to be best synthetic route to obtain single crystals of $Ca_9(Zn_{1-x}In_x)_4Sb_9$. Subsequent flux growth attempts were made using a Zn:In ratio closer to the observed 4:1 stoichiometry. However, these growths yielded crystals of the related (but not isostructural) Zintl phase, $Ca_9Zn_{4+x}Sb_9$ [13], from an identical temperature profile. Use of excess of In is clearly beneficial, since the more Zn-rich fluxes we attempted only grew $Ca_9Zn_{4+x}Sb_9$ crystals, confirming the findings from Ref. [13] that Zn flux readily affords large crystals of the said phase. Reactions with the elements as starting materials, without forming precursors, yielded another, yet unidentified phase.

Single crystals formed by the method decribed in this section were long rods/fibers and possessed a metallic luster. The morphology of some representative crystals is shown in Fig. 1. They were found to be stable in air for at least several weeks.

2.2. Morphology and composition analysis

Scanning electron microscopy was performed on a Tescan Mira 3XMH. Samples were placed on conducting carbon tape to dissipate any residual charge accumulation. Energy-dispersive X-ray spectroscopy (EDX) was performed using an EDAX Apollo X module within the same system. Images were collected and processed with the TEAM software suite.

2.3. Single-crystal X-ray diffraction and structure determination

Single-crystal X-ray diffraction data were collected on a Bruker APEX II CCD-based diffractometer, using monochromated Mo Kα radiation (λ = 0.71073 Å). The operating temperature was 200(2) K, maintained by a cold nitrogen stream. Crystals were selected under a microscope and cut to suitable sizes (ca. 0.1 mm in all dimensions). Many crystals were tried and evaluated by rapid scans, before the best were chosen for full data collection.

Data were acquired in batch runs at varied ω and θ, and were integrated using the SAINT software [23], multi-scan absorption correction was performed using SADABS [24]. Crystal structures were solved with the ShelXT program using the intrinsic phasing solution method and were refined using full-matrix least squares minimization on F^2 with the aid of ShelXL [25,26]. Atomic coordinates were standardized using STRUCTURE TIDY [27]. Details of the data collection, and selected crystallographic parameters are summarized in Tables 1 and 2, as well as Tables S1, S2, S3, S4, and S5 in the supporting information section. Crystallographic information files (CIFs) have been deposited with CSD numbers 2044053–2044055.

2.4. Powder X-ray diffraction

Single crystals grown by the flux method were selected and crushed into fine powder using a mortar and pestle. Powder X-ray diffraction patterns were collected on a Rigaku Smartlab X-ray diffractometer using monochromated Cu Kα radiation (λ = 1.5406 Å) and on a Rigaku

Table 1
Selected data collection details and crystallographic data for $Ca_9Zn_{3.14(3)}In_{0.88}Sb_9$; crystal **(1)** hereafter. Space Group $P\bar{6}2m$, Z = 1, T = 200(2) K, Mo Kα, λ = 0.71073 Å.

Chemical formula	$Ca_9Zn_{3.14(3)}In_{0.88}Sb_9$
fw/g·mol^{-1}	1762.77
a/Å	12.6573(17)
c/Å	4.5356(6)
V/Å^3	629.29(19)
$\rho_{calc.}$/g cm^{-3}	4.65
$\mu_{MoK\alpha}$/cm^{-1}	150.2
R_1 [$I > 2\sigma_{(I)}$][a]	0.0296
wR_2 [$I > 2\sigma_{(I)}$][a]	0.0627
R_1 (all data)[a]	0.0348
wR_2 (all data)[a]	0.0644
$\Delta\rho_{max,min}$/e·Å^{-3}	1.30, −0.83

[a] $R_1 = \sum||F_o|-|F_c||/\sum|F_o|$; w$R_2 = [\sum[w(F_o^2-F_c^2)^2]/\sum[w(F_o^2)^2]]^{1/2}$, where $w = 1/[\sigma^2F_o^2 + (0.0350P)^2]$, and $P = (F_o^2+2F_c^2)/3$.

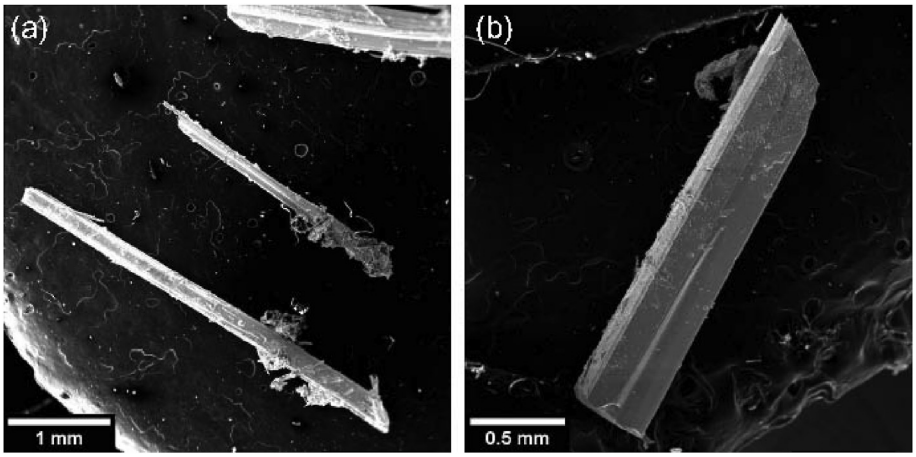

Fig. 1. Needle-like morphology of $Ca_9(Zn_{1-x}In_x)_4Sb_9$ crystals observed using scanning electron microscopy.

Table 2
Atomic coordinates and equivalent displacement parameters (Å^2) for **(1)**.

Atom	Site	*x*	*Y*	*z*	U_{eq}[c]
Ca1	6*j*	0.1822(4)	0.4728(4)	0	0.041(1)
Ca2	3*g*	0.8145(3)	0	1/2	0.019(1)
Zn1/In1[a]	6*k*	0.0738(3)	0.5573(3)	1/2	0.022(1)
Zn2[b]	3*f*	0.1950(6)	0	0	0.023(3)
Sb1	3*g*	0.3002(1)	0	1/2	0.015(1)
Sb2	3*f*	0.6228(1)	0	0	0.029(1)
Sb3	2*d*	1/3	2/3	1/2	0.016(1)
Sb4	1*a*	0	0	0	0.015(1)

[a] Refined occupancies for the mixed-occupied Zn–In site = 0.353(11)Zn + 0.147In.
[b] Refined occupancy for the partially occupied interstitial Zn2 site: 0.341(10).
[c] U_{eq} is defined as one third of the trace of the orthogonalized U_{ij} tensor.

Miniflex diffractometer utilizing filtered Cu Kα radiation ($\lambda = 1.5418$ Å). The GSAS II software [28] was used to analyze the Smartlab data, while the MiniFlex data were only visually compared and matched to the theoretically generated pattern.

2.5. Thermoelectric transport measurements

Electrical resistivity measurements were carried out on two crystals from 80 to 320 K using a custom-built cryostat system based on a standard four-terminal resistance configuration with an applied current of 0.75 mA. Single crystals were mounted on an insulating surface with GE varnish. Electrical contacts were made with Pelco colloidal silver liquid (Ted Pella) and insulated single strand Cu wire (dia. = 0.07 mm).

Thermopower was measured for two crystals in the temperature range 300–600 K (note, these were not the same crystals used for resistivity measurements). Data were gathered with the MMR-Technologies SB-100 module using the integral method and a constantan wire as reference material. Then, constantan wire of the same length and diameter as the sample were mounted on the ceramic stage, which was placed in a temperature-variable chamber (MMR Tech.) and evacuated to ca. 10×10^{-3} torr.

2.6. TG-DSC measurements

Simultaneous thermogravimetry/differential scanning calorimetry measurements (TG/DSC) were conducted on a TA Instruments SDT Q600 analyzer with samples loaded into capped alumina pans. After equilibration at 323 K, the temperature was increased to 1073 K at a rate of 20 K/min. To prevent oxidation, measurements were completed under a constant flow of high-purity argon. DSC data did not indicate any intrinsic thermal events up to ca. 950 K (see Fig. S1 in the Supporting Information). As the temperature approached 1000 K, the sample begins to display poor thermal stability, as demonstrated by the significant mass loss.

3. Results and discussion

3.1. Structural description

Several data sets for a multitude of crystals from different reaction batches were collected during this study. It must be noted that the actual structure of $Ca_9(Zn_{1-x}In_x)_4Sb_9$ is heavily disordered. Depending on the synthetic conditions, partial local ordering is possible, yet, attempts to find a long-range ordered structural model have thus far been unsuccessful. Because of this, the novel structure type represented by $Ca_9(Zn_{1-x}In_x)_4Sb_9$, when neglecting vacant sites, is tentatively assigned as having hexagonal symmetry with Pearson index *hP*27. Herein, we describe the *average* basic hexagonal structure (**1**) and two possible super-structures that stem from it, denoted as cell (**2**) and cell (**3**). The geometric relationship between the basic sub-cell and the two super-structure cells is illustrated schematically by the red (**1**), blue (**2**) and green (**3**) cells in Fig. 2.

After an initial screening for quality, the diffraction data was readily solved using the non-centrosymmetric space group $P\bar{6}2m$ (cell (**1**), described in Table 1). However, synthesized precession images produced weak reflections which are not described by this unit cell. We were able to index a three-fold hexagonal superstructure (**2**) represented schematically by the blue cell in Fig. 2. Despite the tripling of the cell volume in the latter model, and despite the fact that the occupancy of the Zn2 site was very close to 1/3 in model (**1**), an ordered structure could not be obtained with (**2**).

Another dataset collected from a different crystal posed the same problem—it was possible to index all strong reflections in the small hexagonal unit cell, but selecting low intensity reflections suggestive of an ortho-hexagonal distortion of the already deduced super-cell and additional doubling of the cell volume. The orthorhombic superstructure (**3**) is represented by the green cell in Fig. 2, however, extensive disorder on multiple sites persisted, even in this 6 × larger supercell. We note that powder diffraction data collected from a ground batch of crystals yielded peaks consistent with the basic hexagonal unit cell (**1**), but also exhibited additional smaller peaks that could not be fully described by either superstructure model.

In the following paragraphs, the basic average hexagonal structure is detailed, and brief referencing will be made to the partially resolved larger structural fragments, that were discerned in the superstructures (Table S1). In the hexagonal space group $P\bar{6}2m$ (No. 189), there are eight crystallographically unique atoms in the asymmetric unit, all of which occupy special positions with $z = 0$ or $z = 1/2$. Six of the eight atomic sites were readily identified as being occupied by Ca and Sb atoms (Table 2). Based on distances and coordination environments, the remaining two sites were tentatively assigned as Zn1 (6*k*) and Zn2 (3*f*), although subsequent structure refinements revealed significant

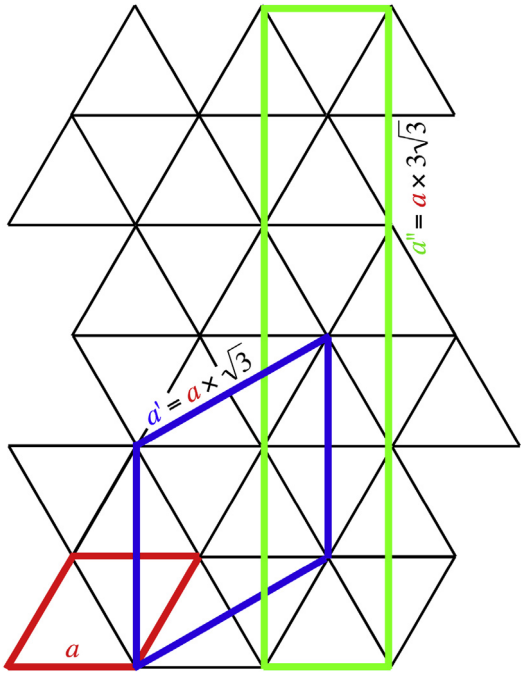

Fig. 2. Crystallographic relationship between the hexagonal sub-cell (crystal **1**, red outline) and two of its possible super-cells, identified from crystallographic work for crystal **2** (blue outline), and crystal **3** (green outline). The corresponding periodicity constants, determined experimentally, are as follows: (**1**) *a* = 12.657 Å; (**2**) *a*' = 21.924 Å; (**3**) *a*'' = 65.694 Å . Further structural details can be found in Table 1 (main text) and Table S1 (supporting information). (For interpretation of the references to color in this figure legend, the reader is referred to the Web version of this article.)

deficiencies of such model; they are elaborated in the following paragraph.

Fig. 3 shows a representation of the structure if all eight sites were fully occupied. Such an idealized structure will have a formula $Ca_9Zn_9Sb_9$ (with one formula unit per unit cell). From the projected view, however, we see that two symmetry-equivalent Zn1 atoms are separated by a nonphysical distance of 1.6 Å. Fixing the occupancy of the Zn1 site at 50% leads to a chemical formula of $Ca_9Zn_6Sb_9$. However, this constraint introduced an excess of electron density on the Zn1 site with a persistent large hole present on the Zn2 site. Freeing the occupation factor of the latter revealed that it was only occupied approximately 1/3 of the time. The excess electron density on the Zn1 site was modeled with a Zn:In ratio of 2:1. This model was successfully refined to a flat and featureless difference Fourier map, with a final refined composition of $Ca_9Zn_{3.1}In_{0.9}Sb_9$. This composition is in excellent agreement with the EDX results.

The reasons for the under-occupation of the Zn2 position are not geometric (i.e., there are no unreasonably short distances involving Zn2) and the coordination environment is fitting for Zn [16,29]. Placing In atoms alone at this position would have resulted in an occupation factor of less than 20% and was ruled out on the basis of the EDX results and the electron count following the Zintl concept, described below. For the same reasons, we did not consider this site to be mixed occupied. Modeling of the superstructures (Table S1) used the same rationale—applying similar constraints to the models resulted in the chemical formulae which matched very close the final refined formula given in Table 1 for the basic sub-cell.

In the most simple terms, the new structure described herein can be broken down to nine Ca^{2+} cations and a $[T_4Sb_9]^{18-}$ (T = mixed Zn/In) polyanion of corner-shared TSb$_4$ tetrahedra and trigonal-planar ZnSb$_3$ fragments (Fig. 3). As mentioned previously, the mixed Zn/In site must be no more than 50% occupied. The random distribution of the vacancies over the crystal may lead to the formation of four different bonding scenarios around three-fold Sb3 atoms, which are schematically depicted in Fig. 4(a). The actual fragments may be conjoined via corner-sharing into chains running along the hexagonal c-axis.

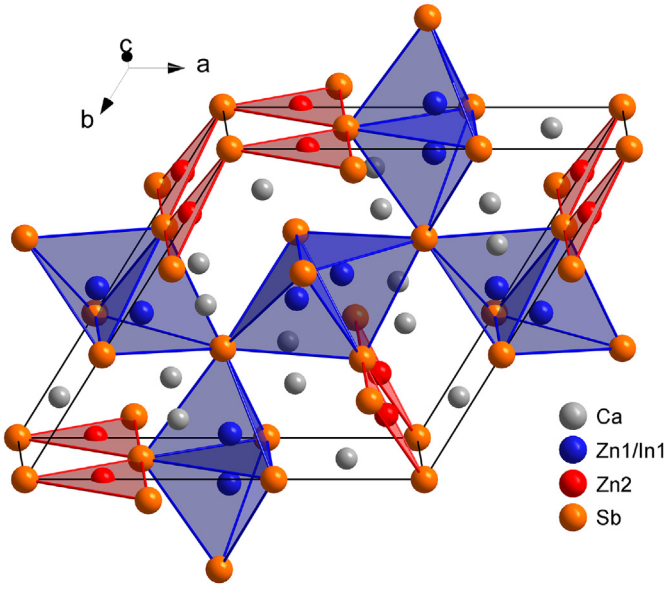

Fig. 3. Average crystal structure of $Ca_9(Zn_{1-x}In_x)_4Sb_9$, viewed approximately along the c-axis. The Ca^{2+} cations are drawn as dark-grey. The mixed Zn1/In1 sites (T), partially occupied Zn sites, and Sb atoms forming complex polyanionic $[T_4Sb_9]$ agglomerate of corner sharing TSb$_4$ tetrahedra and ZnSb$_3$-triangles are shown as blue, red, and orange spheres, respectively. (For interpretation of the references to color in this figure legend, the reader is referred to the Web version of this article.)

[TSb$_4$]-, [T_2Sb$_7$]-, and [T_3Sb$_{10}$]-units are well known and occur in pnictide-based Zintl phases [12]. For instance, [TSb$_4$]-infinite chains are the polyanionic motif in the compounds adopting the Ca_3InP_3 structure type [2,30–32], and [T_2Sb$_7$]-moieties are a part of the ribbons of the structure of all "9-4-9" phases [13,33–36]. The [T_3Sb$_{10}$]-unit of polyanionic sub-lattice has recently been described as a possible structural block for the heavily disordered structures of $Ca_8REMn_{4+x}Sb_9$ (RE = La–Sm) [37]. Similar structural fragments have been reported in β-Ca_2CdAs_2 as well [38].

The Zn2 position, shown in Fig. 4(b), is three-fold coordinated, situated in the center of a triangle formed by Sb atoms. These triangles form tri-star shaped infinite ribbons, interconnected through Sb4 atoms, and oriented along the c-axis as shown in Fig. 4(d). Planar coordination is uncommon for Zn, however, there is precedent for Zn atoms in trigonal planar environments with the most relevant being the Zn-based Zintl phases adopting the Ca_2ZnP_2 structure (defect ZrBeSi type) [16]. The difference between the title compound and mentioned "2-1-2" phases is related to the occupancy of the interstitial Zn atom. The latter show half-occupied Zn, whereas in the present case, the Zn occupancy is 1/3. [ZnSb$_3$] units are also part of the anionic sub-lattices in most of the Zn-based "9-4-9" phases (Fig. 5) [13]. For instance, an interstitial Zn3 site in $Ca_9Zn_{4+x}Sb_9$ is partially occupied with the refined occupancy range of approximately 11–24% forming ribbon-like one-dimensional [ZnSb$_3$] chains, which bridge $[Zn_4Sb_9]^{19-}$ chains into a two-dimensional channel-like structure.

The interstitial Zn3 site is a hallmark of the $Ca_9Zn_{4+x}Sb_9$ structure, which differentiates the structure from the parent $Ca_9Mn_4Bi_9$ structure type. The only difference between the [ZnSb$_3$] fragment in $Ca_9(Zn_{1-x}In_x)_4Sb_9$ compared to that in $Ca_9Zn_{4+x}Sb_9$ is that in the latter, the interstitial Zn atom is situated slightly above the Sb3 triangle (Fig. 5(d)), whereas the Zn2 atom in the presently discussed compound is located precisely within the plane of the three neighboring Sb atoms (Fig. 4(b)), similar to that in Ca_2ZnP_2 [16].

The local coordination environment of the two Ca atoms can be described as distorted octahedral (Fig. 4(c)). Relevant interatomic distances are presented in Table 3. Most of the Ca–Sb distances are close to the simple sum of the covalent radii of Ca and Sb [39]. However, one of the Ca1–Sb2 contacts (3.647 Å) is significantly longer. With this in mind, a distorted square-pyramidal coordination for Ca1 might be a more apt description. In the orthorhombic structure of $Ca_9Zn_{4+x}Sb_9$, two of the Ca atoms also have such long Ca–Sb contacts. Similar distortions of the Ca-octahedra are present in the monoclinic $Ca_{21}Zn_4Sb_{18}$ and the tetragonal $Ca_{14}Zn_{1+x}Sb_{11}$ [18,29,40], which is suggestive that local structural deviations from the global hexagonal symmetry are very likely.

Due to the smaller covalent radius of Zn (r_{Zn} = 1.22 Å) in comparison to In (r_{In} = 1.42 Å) [39], and the different coordination numbers, the Zn1/In1–Sb bonds (2.73–2.91 Å) are longer than the Zn2–Sb bonds (2.47–2.63 Å). These distances are comparable to those in previously reported In/Zn–Sb compounds, such as $Ca_{14}Zn_{1+x}Sb_{11}$ [18], $Ca_9Zn_{4+x}Sb_9$ [13], $Ca_{21}Zn_4Sb_{18}$, and $Ca_5In_2Sb_6$ [40–42]. The Sb–Zn/In–Sb angles slightly deviate from the ideal tetrahedral angle (109.5°), which also supports the notion of a flexible coordination geometry.

3.1.1. Structural relationships

In this section, the structural relationships between the hexagonal sub-cell (**1**) and two complex superstructures (**2**) and (**3**) will be briefly described. As can be seen from Tables S2 and S4, and Fig. 5, both superstructures partially resolve the disorder. The hexagonal superstructure (**2**) is a 3-fold superstructure of (**1**). It still contains face-sharing TSb$_4$ (T = Zn/In) tetrahedra, which cannot be present simultaneously. The multiplicity of the Zn/In site in the sub-cell was lowered from 6k to 3k in the supercell. As a result, the split position consists of both Zn and In (Table S3). Two more TSb$_4$ tetrahedra are corner-shared and exhibit a mixed occupation of the central atom. One of the possible basic structural fragments describing the crystal structure of the hexagonal sub-cell (**1**) is

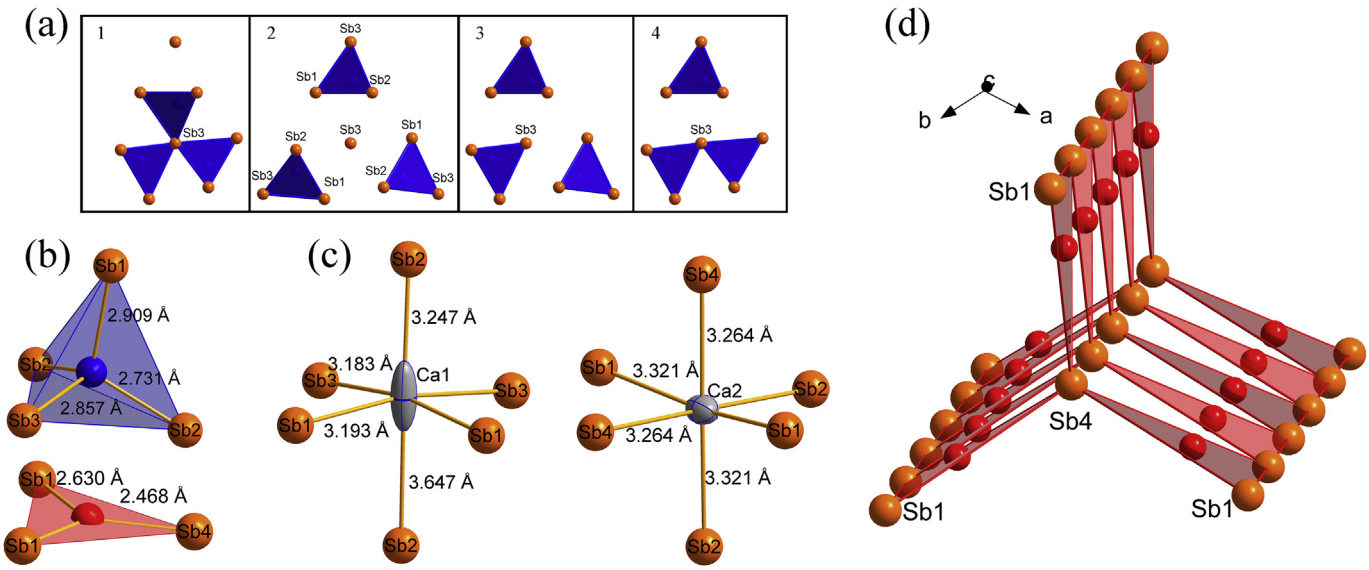

Fig. 4. (a) Possible structural fragments in the *average* crystal structure of $Ca_9(Zn_{1-x}In_x)_4Sb_9$. Hexagonal supercell (**2**) suggests that (a-3) and (a-4) patterns are most likely (see Fig. 5(b)). (b) Coordination polyhedrons of the mixed Zn/In site (blue) and partially occupied Zn2 site (red). (c) Local coordination environment of two Ca atoms; the elongated thermal ellipsoid of Ca1 can be correlated with the significant axial distortion of the octahedron. (d) $[ZnSb_3]$ is the second anionic structural fragment of the sub-lattice. Superposition of (a) and (d) fragments forms the overall crystal structure deduced based on the sub-cell (**1**). Color code is the same as in Fig. 3. (For interpretation of the references to color in this figure legend, the reader is referred to the Web version of this article.)

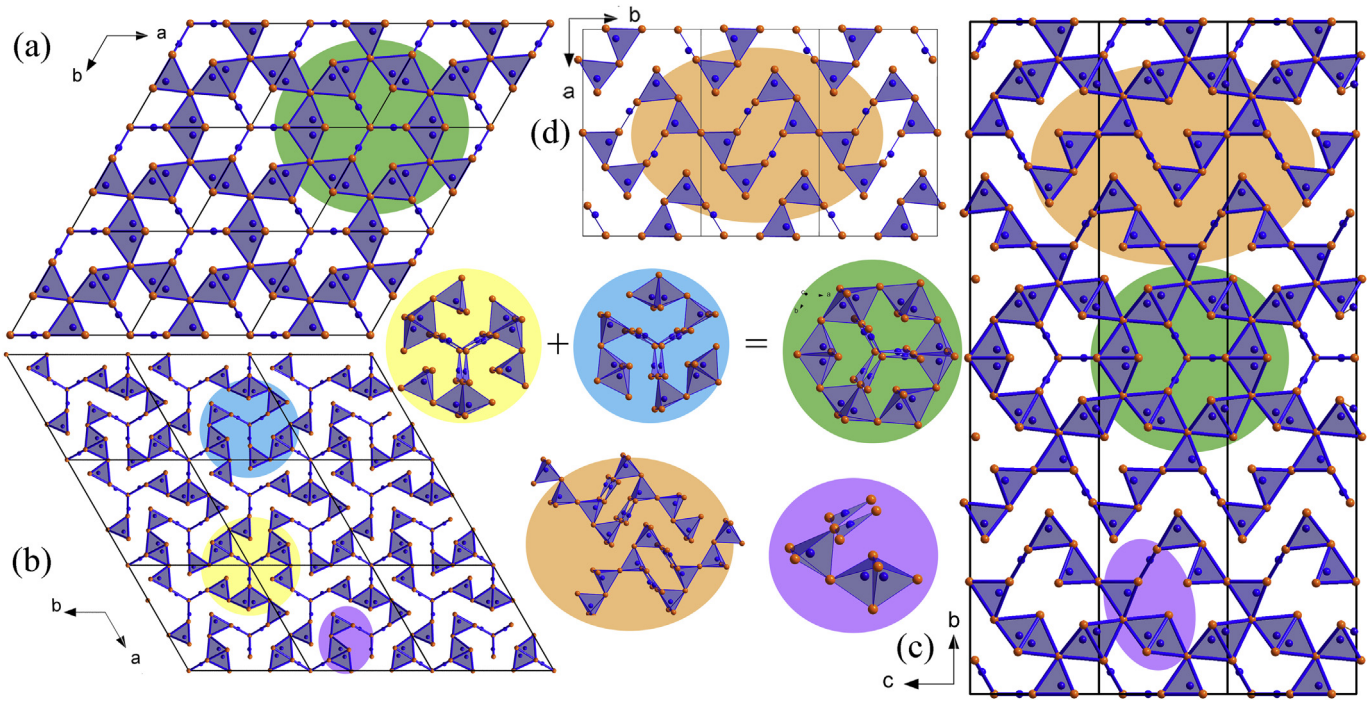

Fig. 5. Polyhedral representation of structures (**1**) (small hexagonal sub-cell, shown in panel a); (**2**) (hexagonal superstructure shown in panel b); and (**3**) (orthorhombic superstructure shown in panel c). (d) The structure of the closely related orthorhombic $Ca_9Zn_{4+x}Sb_9$. The unit cells are outlined. Ca atoms are omitted for clarity in all structures. The Sb atoms are drawn in orange, all Zn/In and Zn-based polyhedral units are in blue. Structural relationships between all presented structures are emphasized through close up views of the complex polyanionic fragments with the colored backgrounds. All Zn/In-based face-sharing tetrahedra are always split and occur as a single fragment, due to the short Zn/In–Zn/In interatomic contact. Trigonal-planar coordinated Zn atoms are always partially occupied. (For interpretation of the references to color in this figure legend, the reader is referred to the Web version of this article.)

the complex agglomerate emphasized by the green background in Fig. 5. It is not present in the current form in the superstructure (**2**) due to the lower symmetry. However, the superposition of two other, rather similar structural fragments (on the yellow and blue background) leads to the formation of such agglomerates. The latter is one of the two slabs in the orthorhombic superstructure (**3**).

The second slab in the orthorhombic structure can be recognized as a fragment from the $Ca_9Mn_4Bi_9$ structure type, consisting of all-corner shared units (orange background), isosteric with the $[Mn_4Bi_9]$ double chains. However, a more careful look shows that the connectivity is subtly different. It rather resembles the structure of $Ca_9Zn_{4+x}Sb_9$ (Fig. 5(d)), where two $[Zn_4Sb_{13}]$ ribbons are connected by interstitial Zn

Table 3
Selected interatomic distances (Å) in **(1)**.

Atom pair	Distance/Å
Ca1–Sb1 × 2	3.193(3)
Ca1–Sb2	3.246(5)
	3.648(5)
Ca1–Sb3 × 2	3.183(3)
Ca2–Sb1 × 2	3.321(1)
Ca2–Sb2 × 2	3.321(3)
Ca2–Sb4 × 2	3.264(3)
Zn1/In1–Sb1	2.909(3)
Zn1/In1–Sb2 × 2	2.731(2)
Zn1/In1–Sb3	2.858(3)
Zn2–Sb1 × 2	2.630(4)
Zn2–Sb4	2.468(7)

atoms (which form infinite $[ZnSb_3]$ layers). From the above, given that crystal growth conditions greatly influence the interpretation of the diffraction data, it can be proposed that the local structure of $Ca_9(Zn_{1-x}In_x)_4Sb_9$ boasts the following three structural fragments: (a) the typical $[T_4Sb_{13}]$ ribbons interconnected by a single interstitial Zn atom; (b) $[T_3Sb_{10}]$ ribbons, in case $[TSb_4]$tetrahedron is randomly located close to the ribbon; (c) $[T_5Sb_{16}]$agglomerate, similar to that in the β-Ca_2CdAs_2 structure. It can be imagined as a combination of $[T_3Sb_{10}]$ ribbon, extended by the structural fragment displayed in Fig. 4(b).

3.1.2. Electron count

As discussed elsewhere [13], the prototypical Zn-based "9-4-9" phases are electron-deficient on the basis of the Zintl-Klemm rules. Given that there is no homo-atomic Sb–Sb bonding, the valence electrons in an idealized $Ca_9Zn_4Sb_9$ will be partitioned as follows:

$$Ca_9Zn_4Sb_9 = (Ca^{2+})_9(Zn^{2+})_4(Sb^{3-})_9(h^+),$$

where (h^+) denotes an electron-hole. This is done with the assumption that the backbone of the structure, the $ZnSb_4$ tetrahedra, feature interactions which are simple 2-center-2-electron bonds. Apparently this electronic instability can be alleviated by the addition of a partially occupied interstitial Zn site with formula $Ca_9Zn_{4+x}Sb_9$ ($x = 0.5$), the structure becomes valence-precise:

$$Ca_9Zn_{4.5}Sb_9 = (Ca^{2+})_9(Zn^{2+})_{4.5}(Sb^{3-})_9.$$

In the current case of $Ca_9(Zn_{1-x}In_x)_4Sb_9$, the structure has found yet another mechanism to bring the valence electron count closer to ideal (actual electronic structure calculations to confirm this are not feasible since even in the largest worked out superstructure (**3**), there is still extensive disorder). The aliovalent Zn^{2+}/In^{3+} partial substitution allows for the following structure rationalization:

$$Ca_9Zn_3InSb_9 = (Ca^{2+})_9(Zn^{2+})_3(In^{3+})(Sb^{3-})_9$$

The experimentally refined composition $Ca_9Zn_{3.1}In_{0.9}Sb_9$ is indeed very close to the ideal case, which considering the fact that the crystals were always obtained from a very In-rich melt, is indirect evidence that the synthesized material represents the limiting solubility of In metal in $Ca_9(Zn_{1-x}In_x)_4Sb_9$. This conclusion is in-line with the other recently reported case of aliovalent Mn^{2+}/Al^{3+} substitution in $Eu_9(Mn_{1-x}Al_x)_4Sb_9$ ($x \approx 1.1$), which is at a comparable level [36].

3.2. Electronic transport

Resistivity measurements of two in $Ca_9(Zn_{1-x}In_x)_4Sb_9$ crystals were performed as a function of temperature in the range of 80–320 K as shown in Fig. 6(a). The measurements were taken parallel to the long direction of the crystals (parallel to the *c*-axis of the average hexagonal unit cell). Both samples were found to have resistivity that increases by more than 50% over the measured temperature range. The resistivity at room temperature of approx. 1 mΩ cm is comparable to the resistivity of

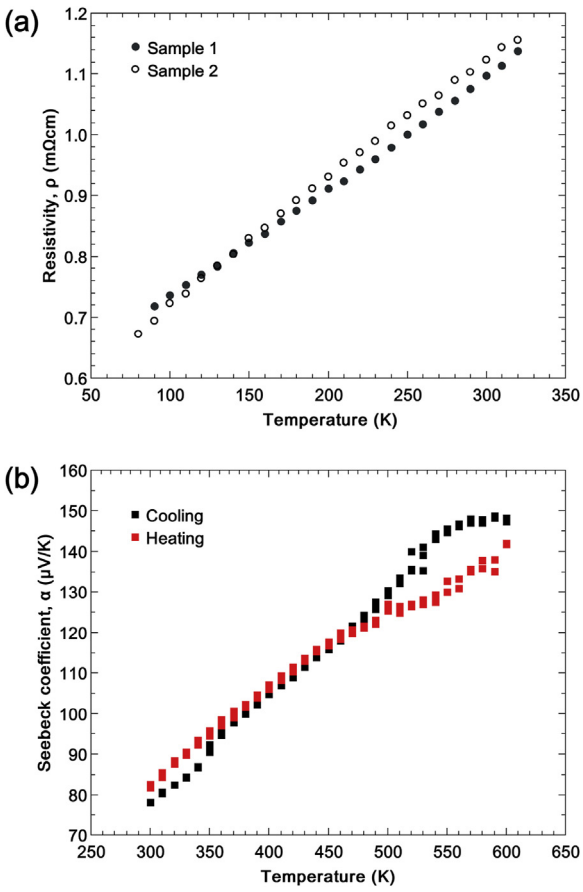

Fig. 6. Temperature dependence of resistivity (top) and Seebeck (bottom) for single crystal $Ca_9(Zn_{1-x}In_x)_4Sb_9$, indicative of intrinsic semiconducting and *p*-type behavior.

many optimized thermoelectric materials. The Seebeck coefficient, *S*, measured from 300 to 600 K is shown in Fig. 6(b). As with the conductivity, *S* was also measured parallel to the longest dimension of the crystals. The positive, linearly increasing Seebeck coefficients indicate that the crystals are degenerate *p*-type semiconductors. In particular, the magnitude of the Seebeck coefficient at high temperature, up to a maximum of 150 μV/K at 600 K, is sufficiently high to indicate that the compound is indeed semiconducting, as opposed to semimetallic (i.e., zero band gap). Using the Goldsmid-Sharp approximation ($E_g = 2S_{max}T_{max}$, where S_{max} is the maximum Seebeck coefficient), we estimate a band gap of approximately 0.2 eV. The degenerate *p*-type behavior suggests that the stoichiometry of these crystals deviates slightly from the valence-precise composition ($Ca_9Zn_3InSb_9$). The refined stoichiometry of $Ca_9Zn_{3.1}In_{0.9}Sb_9$ would be expected to lead to a significant free hole concentration, consistent the observed *p*-type conduction.

At room temperature, the resistivity and Seebeck coefficients of the $Ca_9(Zn_{1-x}In_x)_4Sb_9$ crystals are both comparable to that of $Ca_9Zn_{4+x}Sb_9$ samples ($x = 0.2$–0.4), which were reported to have $zT \approx 1$ [22]. Given the degree of disorder in the structure of the current system, we would expect to measure lattice thermal conductivity of 1 W/m K or less. These results suggest that this new $Ca_9(Zn_{1-x}In_x)_4Sb_9$ Zintl phase is likely to exhibit a promising thermoelectric figure of merit, given optimization of the synthesis conditions for bulk samples as well as fine tuning of the carrier concentration. In the case of the $Ca_9Zn_{4+x}Sb_9$, small changes in the Zn content, *x*, were used to control the carrier concentration. In the present system, it may be possible to control the carrier concentration using a similar approach, or by slightly varying the Zn:In ratio.

4. Conclusions

Two new ternary *n*-type semiconducting Zintl phases have been synthesized using Synthesis and characterization of the newly discovery quaternary compound $Ca_9Zn_{3.1}In_{0.9}Sb_9$ was conducted. A hexagonal subcell and two complex superstructures were resolved to describe the heavily disordered structure. Structural fragments of the new structure type resemble that of other "9-4-9" compositions, such as $Ca_9Zn_{4+x}Sb_9$, but valence balance is achieved uniquely through the aliovalent Zn^{2+}/In^{3+} partial substitution. Resistivity and Seebeck coefficient measurements exhibited low linear behavior consistent with degenerate *p*-type semiconducting behavior, and confirm that the compound possesses a non-zero band gap. The experimental transport properties suggest that $Ca_9Zn_{3.1}In_{0.9}Sb_9$ has the potential to be an excellent new thermoelectric material, with performance comparable to the related $Ca_9Zn_{4+x}Sb_9$ compound).

CRediT authorship contribution statement

David M. Smiadak: Writing - original draftWriting – original draft, Synthesis and Material Property Characterization, Writing. **Sviatoslav Baranets:** Investigation, Methodology, Formal analysis, Writing - original draftWriting – original draft. **Megan Rylko:** Aid with Synthesis and Preliminary Characterization. **Mack Marshall:** Aid with Synthesis and Preliminary Characterization. **Mario Calderón-Cueva:** Aid with Synthesis and Preliminary Characterization. **Svilen Bobev:** Conceptualization, Supervision, Project administration, Writing - review & editingWriting – review & editing. **Alex Zevalkink:** Conceptualization, Project administration, Writing - review & editingWriting – review & editing.

Declaration of competing interest

The authors declare that they have no known competing financial interests or personal relationships that could have appeared to influence the work reported in this paper.

Acknowledgments

Synthesis and characterization performed at Michigan State University were supported by the National Science Foundation (NSF) award number 1709158. Structural characterization at University of Delaware received financial support from the United States Department of Energy through grant DE-SC0008885.

Appendix A. Supplementary data

Supplementary data to this article can be found online at https://doi.org/10.1016/j.jssc.2020.121947.

References

[1] K.-F. Liu, S.-Q. Xia, Recent progresses on thermoelectric Zintl phases: structures, materials and optimization, J. Solid State Chem. 270 (2019) 252–264.
[2] A. Zevalkink, E. Toberer, W. Zeier, E. Flage-Larsen, G.J. Snyder, Ca_3AlSb_3: an inexpensive, non-toxic thermoelectric material for waste heat recovery, Energy Environ. Sci. 4 (2) (2010) 510–518.
[3] W. Zeier, A. Zevalkink, E. Schechtel, W. Tremel, G.J. Snyder, Thermoelectric properties of Zn-doped Ca_3AlSb_3, J. Mater. Chem. 22 (19) (2012) 9826–9830.
[4] D. Young, S. Kauzlarich, Preparation, structure, and electronic properties of $Ca_{11}MSb_9$ (M = Al, Ga, In), Chem. Mater. 7 (1) (1995) 206–209.
[5] E. Toberer, A. Zevalkink, N. Crisosto, G.J. Snyder, The Zintl compound $Ca_5Al_2Sb_6$ for low-cost thermoelectric power generation, Adv. Funct. Mater. 20 (24) (2010) 4375–4380.
[6] A. Zevalkink, E. Toberer, T. Bleith, E. Flage-Larsen, G.J. Snyder, Improved carrier concentration control in Zn-doped $Ca_5Al_2Sb_6$, J. Appl. Phys. 110 (1) (2011) 13721.
[7] A. Zevalkink, G. Pomrehn, S. Johnson, J. Swallow, Z. Gibbs, G.J. Snyder, Influence of the triel elements (M = Al, Ga, In) on the transport properties of $Ca_5M_2Sb_6$ Zintl compounds, Chem. Mater. 24 (11) (2012) 2091–2098.
[8] S. Johnson, A. Zevalkink, G.J. Snyder, Improved thermoelectric properties in Zn-doped $Ca_5Ga_2Sb_6$, J. Mater. Chem. 1 (13) (2013) 4244.
[9] Y. Hu, G. Cerretti, E.L. Kunz-Wille, S.K. Bux, S.M. Kauzlarich, The remarkable crystal chemistry of the $Ca_{14}AlSb_{11}$ structure type, magnetic and thermoelectric properties, J. Solid State Chem. 271 (2019) 88–102.
[10] R. Nesper, The Zintl-Klemm concept – a historical survey, Z. Anorg. Allg. Chem. 640 (14) (2014) 2639–2648.
[11] E.S. Toberer, A. Zevalkink, G.J. Snyder, Phonon engineering through crystal chemistry, J. Mater. Chem. 21 (40) (2011) 15843.
[12] A. Ovchinnikov, S. Bobev, Zintl phases with group 15 elements and the transition metals: a brief overview of pnictides with diverse and complex structures, J. Solid State Chem. 270 (2019) 346–359.
[13] S. Bobev, J.D. Thompson, J.L. Sarrao, M.M. Olmstead, H. Hope, S.M. Kauzlarich, Probing the limits of the Zintl concept: structure and bonding in rare-earth and alkaline-earth zinc-antimonides $Yb_9Zn_{4+x}Sb_9$ and $Ca_9Zn_{4.5}Sb_9$, Inorg. Chem. 43 (16) (2004) 5044.
[14] S. Bobev, V. Fritsch, J.D. Thompson, J.L. Sarrao, B. Eck, R. Dronskowski, S.M. Kauzlarich, Synthesis, structure and properties of the new rare-earth Zintl phase $Yb_{11}GaSb_9$, J. Solid State Chem. 178 (4) (2005) 1071–1079.
[15] B. Saparov, S. Bobev, A. Ozbay, E.R. Nowak, Synthesis, structure and physical properties of the new Zintl phases $Eu_{11}Zn_6Sb_{12}$ and $Eu_{11}Cd_6Sb_{12}$, J. Solid State Chem. 181 (10) (2008) 2690–2696.
[16] D.K. Wilson, B. Saparov, S. Bobev, Synthesis, crystal structures and properties of the Zintl phases Sr_2ZnP_2, Sr_2ZnAs_2, A_2ZnSb_2 and A_2ZnBi_2 (A = Sr and Eu), Z. Anorg. Allg. Chem. 637 (13) (2011) 2018–2025.
[17] S. Stoyko, L. Voss, H. He, S. Bobev, Synthesis, crystal and electronic structures of the pnictides AE_3TrPn_3 (AE = Sr, Ba; Tr = Al, Ga; Pn = P, As), Crystals 5 (2015) 433–446.
[18] S. Baranets, S. Bobev, From the ternary phase $Ca_{14}Zn_{1+\delta}Sb_{11}$ ($\delta \approx 0.4$) to the quaternary solid solutions $Ca_{14-x}RE_xZnSb_{11}$ (RE = La–Nd, Sm, Gd, $x \approx 0.9$). A tale of electron doping via rare-earth metal substitutions and the concomitant structural transformations, Inorg. Chem. 58 (13) (2019) 8506–8516.
[19] A. Wang, S. Baranets, Y. Liu, X. Tong, E. Stavitski, J. Zhang, Y. Chai, W.-G. Yin, S. Bobev, C. Petrovic, Magnetic mixed valent semimetal $EuZnSb_2$ with Dirac states in the band structure, Phys. Rev. Resear. 2 (2020), 033462.
[20] G. Dhanaraj, Springer Handbook of Crystal Growth, first ed., Springer Verlag, 2010.
[21] P. Canfield, T. Kong, U. Kaluarachchi, N. Jo, Use of frit-disc crucibles for routine and exploratory solution growth of single crystalline samples, Philos. Mag. A 96 (1) (2016) 84–92.
[22] S. Ohno, U. Aydemir, M. Amsler, J. Pöhls, S. Chanakian, A. Zevalkink, M.A. White, S.K. Bux, C. Wolverton, G.J. Snyder, Achieving $zT > 1$ in inexpensive Zintl phase $Ca_9Zn_{4+x}Sb_9$ by phase boundary mapping, Adv. Funct. Mater. 27 (20) (2017) 1606361.
[23] Bruker AXS Inc, SAINT (2014).
[24] L. Krause, R. Herbst-Irmer, G.M. Sheldrick, D. Stalke, Comparison of silver and molybdenum microfocus X-ray sources for single-crystal structure determination, J. Appl. Crystallogr. 48 (1) (2015) 3–10.
[25] G.M. Sheldrick, Shelxt – integrated space-group and crystal-structure determination, Acta Crystallogr. A 71 (1) (2015) 3–8.
[26] G.M. Sheldrick, Crystal structure refinement with SHELXL, Acta Crystallogr. C 71 (1) (2015) 3–8.
[27] L.M. Gelato, E. Parthé, Structure TIDY – a computer program to standardize crystal structure data, J. Appl. Crystallogr. 20 (2) (1987) 139–143.
[28] B.H. Toby, R.B. Von Dreele, GSAS-II: the genesis of a modern open-source all purpose crystallography software package, J. Appl. Crystallogr. 46 (2) (2013) 544–549.
[29] S. Baranets, G.M. Darone, S. Bobev, Synthesis and structure of $Sr_{14}Zn_{1+x}As_{11}$ and $Eu_{14}Zn_{1+x}As_{11}$ ($x \leq 0.5$). New members of the family of pnictides isotypic with $Ca_{14}AlSb_{11}$, exhibiting a new type of structural disorder, J. Solid State Chem. 280 (2019) 120990.
[30] G. Cordier, H. Schäfer, M. Stelter, Neue Zintlphasen: Ba_3GaSb_3, Ca_3GaAs_3 und Ca_3InP_3, Z. Naturforsch. B Chem. Sci. 40 (9) (1985) 1100–1104.
[31] J. Jiang, A.C. Payne, M.M. Olmstead, H.-O. Lee, P. Klavins, Z. Fisk, S.M. Kauzlarich, R.P. Hermann, F. Grandjean, G.J. Long, Complex magnetic ordering in Eu_3InP_3: a new rare earth metal Zintl compound, Inorg. Chem. 44 (7) (2005) 2189–2197.
[32] K. Rajput, S. Baranets, S. Bobev, Observation of an unexpected n-type semiconducting behavior in the new ternary Zintl phase Eu_3InAs_3, Chem. Mater. 32 (2020) 9616–9626.
[33] S.-J. Kim, J. Salvador, D. Bilc, S.D. Mahanti, M.G. Kanatzidis, $Yb_9Zn_4Bi_9$: extension of the Zintl concept to the mixed-valent spectator cations, J. Am. Chem. Soc. 123 (50) (2001) 12704–12705.
[34] S.-Q. Xia, S. Bobev, Interplay between size and electronic effects in determining the homogeneity range of the $A_9Zn_{4+x}Pn_9$ and $A_9Cd_{4+x}Pn_9$ phases ($0 \leq x < \leq 0.5$), A = Ca, Sr, Yb, Eu; Pn = Sb, Bi, J. Am. Chem. Soc. 129 (32) (2007) 10011–10018.
[35] X.-C. Liu, Z. Wu, S.-Q. Xia, X.-T. Tao, S. Bobev, Structural variability versus structural flexibility. A case study of $Eu_9Cd_{4+x}Sb_9$ and $Ca_9Mn_{4+x}Sb_9$ ($x \approx 1/2$), Inorg. Chem. 54 (3) (2015) 947–955.
[36] X.-C. Liu, K.-F. Liu, Q.-Q. Wang, Y.-M. Wang, M.-Y. Pan, S.-Q. Xia, Exploring new Zintl phases in the 9-4-9 family via Al substitution. Synthesis, structure, and physical properties of $Ae_9Mn_{4-x}Al_xSb_9$ (Ae = Ca, Yb, Eu), Inorg. Chem. 59 (6) (2020) 3709–3717.
[37] Y. Wang, S. Bobev, Rare-earth metal substitutions in $Ca_{9-x}RE_xMn_4Sb_9$ (RE = La–Nd, Sm; $x \approx 1$). Synthesis and characterization of a new series of narrow-gap semiconductors, Chem. Mater. 30 (10) (2018) 3518–3527.
[38] J. Wang, M. Yang, M.-Y. Pan, S.-Q. Xia, X.-T. Tao, H. He, G. Darone, S. Bobev, Synthesis, crystal and electronic structures, and properties of the new pnictide

semiconductors A_2CdPn_2 (A = Ca, Sr, Ba, Eu; Pn = P, As), Inorg. Chem. 50 (17) (2011) 8020–8027.
[39] B. Cordero, V. Gómez, A.E. Platero-Prats, M. Revés, J. Echeverría, E. Cremades, F. Barragán, S. Alvarez, Covalent radii revisited, Dalton Trans. 21 (2008) 2832.
[40] N.-T. Suen, Y. Wang, S. Bobev, Synthesis, crystal structures, and physical properties of the new Zintl phases $A_{21}Zn_4Pn_{18}$ (A = Ca, Eu; Pn = As, Sb)—versatile arrangements of [ZnPn_4] tetrahedra, J. Solid State Chem. 227 (C) (2015) 204–211.
[41] G. Cordier, H. Schäfer, M. Stelter, Perantimonidogallate und -indate: zur kenntnis von $Ca_5Ga_2Sb_6$, $Ca_5In_2Sb_6$ und $Sr_5In_2Sb_6$, Z. Naturforsch. 40 (b) (1985) 5–8.
[42] A. Zevalkink, J. Swallow, G. J Snyder, Thermoelectric properties of Zn-doped $Ca_5In_2Sb_6$, Dalton Trans. 42 (26) (2013) 9713–9719.